Robust effects of In, Fe, and Co additions on microstructures, thermal, and mechanical properties of hypoeutectic Sn–Zn-based lead-free solder alloy

A. M. El-Taher[1,*] (iD), S. A. Mansour[2], and I. H. Lotfy[2]

[1] *Physics Department, Faculty of Science, Zagazig University, Zagazig 44519, Egypt*
[2] *Physics Department, Faculty of Science, Suez Canal University, Ismailia 41522, Egypt*

ABSTRACT

This study examines the influence of separate and dual minor alloying additions of indium (In) and ferrous/cobalt (Fe/Co) on the microstructure, thermal, and mechanical properties of hypoeutectic Sn–7wt.% Zn lead-free solder alloy. The results showed that the addition of In resulted in significant refinement in the microstructure and formation of new intermetallic compounds (IMCs) such as In–Sn phases which capable of extensively removing the unfavorable needle-like α-Zn phase. However, the additions of Fe/Co resulted in the creation of new coarsening flower-shaped IMCs identified as Zn–Co, Fe–Sn, and Co–Sn–Zn distributed uniformly which may have a marked effect on the mechanical and thermal properties of Sn–Zn solder alloy. Thermal analysis by a differential scanning calorimeter indicates slightly reduction in the onset temperature, melting temperature, and undercooling of the Sn–7wt.% Zn by the addition of In, while the pasty range enlarged as compared to Fe/Co additions. The tensile tests indicate that the Sn-Zn-In solder alloy exhibited a superior balance of ultimate tensile strength, yield strength, Young's modulus, and elongation of 51.5 MPa, 44.4 MPa, 22.2GPa, and 44.5%, respectively, which are better than both those of the Sn–Zn and Sn–Zn–Fe/Co solder alloys. This can be attributed to the synergistic strengthening mechanism of refinement in the microstructure and precipitation of fine secondary particles.

1 Introduction

Lead-based alloys, such as Sn-Pb, have been traditionally employed in the assembly of microelectronics due to their favorable characteristics, which include low melting point (∼183℃), strong mechanical properties, ease of manufacture, and cost-effectiveness. But concerns have escalated over the use of lead in abundance due to its high toxicity, which is harmful to the environment and humans [1–3]. This challenging issue results in a widespread effort to develop new lead-free Sn-based alloys with

Address correspondence to E-mail: ahmedeltaher80@gmail.com

good mechanical properties. Sn–Zn alloys are considered as potential candidates for use in Pb-free solders in electronics interconnections owing to their low cost, lower melting temperature (198 °C), and superior mechanical characteristics (strength and plasticity) compared to other lead-free solders [4–7]. They have some undesirable properties such as poor corrosion resistance, poor wettability, tendency to oxidize, and micro-void formation owing to the high activity of Zn element, which are significant reliability issue for their industrial implementation [8–10]. There have been multiple efforts to improve the wetting and oxidation properties of Sn-Zn alloys, which have included the incorporation of various elements, such as Ga, Nd, Ti, Al, Cr, In, Ni, Co, Fe, and Bi, into the Sn-Zn alloy composition [11–13]. Chen et al. [8] doped 0.5 and 3wt.% of Ga in Sn-9Zn alloys to improve the oxidation resistance and ensure a better solderability and mechanical property. Hu et al. [9] reported that doping traces of Nd with Sn–9Zn alloys resulted in enrichment and precipitation of Zn, which could significantly enhance the solderability and mechanical characteristic of the solder alloy. Chen et al. [10] showed that microalloying with elements such as Ti, Cr, and Al causes a reduction in the oxidation of Sn-9Zn solder. Mccormack et al. noted that doping 5wt.% In with the Sn-9Zn fusible alloys can reduce the melting point to ∼ 175–188 °C in addition to enhancing the wetting characteristics [11]. Li et al.'s investigation reveals that both interfacial microstructure and shear strength of the Sn–9Zn–Ni interconnections could be enhanced with 3 wt.% Co addition, since Co can impede the formation of Ni_5Zn_{21} and reacts with Zn in the composite solders. [12]. Previous studies indicated that there are two factors that can enhance the Sn–Zn alloys family characteristics are lowering the amount of Zn in the alloy matrix and the additions of a third element. The phase diagram of Sn-Zn reveals that the reduction of Zn content close to the hypoeutectic Sn-6.5Zn will preserve the melting point temperature at its level, i.e., Sn-7Zn exhibits the same advantages of inducing similar melting temperature of the Sn-9Zn solder alloy [13]. Nevertheless, the hypoeutectic Sn-7Zn delivers extremely sufficient wettability to Cu than the eutectic Sn-9Zn, which gives it the advantage of being utilized as a lead-free solder [13–15]. Indium is recognized as a considerable effective element owing to excellent thermal properties and wettability. Therefore, the addition of the In is expected to

preserve the melting point at the same level and increase the mechanical characteristics of the Sn-7Zn system. While Fe is a inexpensive element, it is considered non-hazard materials, and under 200 °C, Fe has a lower solubility in the β-Sn matrix. So, the addition of Fe to the Sn-7Zn system is expected to modify the wetting and mechanical behavior. However, as far as we know, there are no reports on the influence of microalloying of small amount In and Fe/Co on the microstructure and mechanical and thermal properties of Sn-7 wt.%Zn alloy. The present work aims to fill this gap by studying the impact of these additions on the microstructural, thermal, and mechanical characteristics of Sn-7Zn solder alloy.

2 Experimental techniques

The effects of 2.5 wt.% In and traces of Fe and Co (0.1 wt. % for each) on the characteristics of the hypoeutectic Sn-7Zn alloy were investigated in this study. Metal ingots of Sn (99.9%), Zn (99.99%), In, Fe, and Co (99.99%) were used to prepare the investigated binary, ternary, and quaternary alloys. The following steps were followed to prepare the samples: (1) A quartz tube of 25 mm in diameter and 80 mm in height was used as a container of the alloy's mixture under an anti-oxidizing flux of KCl + LiCl (1.3:1). (2) The mixture was molten in an electrical furnace set to ∼ 700 °C for about an hour. (3) To ensure complete alloy dissolution, mechanical stirring with a graphite rod was performed. (4) The molten alloys were poured into a steel mold and allowed to cool naturally with cooling rate 6–8 °C/s, so as to construct microstructures typically creates in small solder joints in electronic industries. The alloy samples were divided into two sections for our investigations: one for the microstructural investigations, which had a cylindrical shape of 1×10^{-2} m in diameter and 1×10^{-2} m m in height, and the other portion was cold drawn to turn into wires for the mechanical investigations. The morphological microstructure of alloy samples was studied using field emission scanning electron microscopy (Quanta FEG 250, USA), while the undercooling values and eutectic temperatures of the solders were defined using differential scanning calorimetry (DSC) (Shimadzu-50 DSC-50, Japan) at temperatures ranging from 30 °C to 227 °C beneath the nitrogen environment, at heating and cooling rates of 10 °C/min. To perform the

tensile tests, the alloy samples were drawn into wires with a marked standard length of 4×10^{-2} m and diameter of 4×10^{-3} m [16]. Then, the investigations were performed at strain rates from 10^{-3} to 10^{-5} s^{-1} and temperatures from 25 to 120 °C using the computerized tensile testing machine system as illustrated earlier [17].

3 Results and discussion

3.1 X-Ray diffractometry analysis

Figure 1 displays the X-ray diffractometry (XRD) patterns for the Sn-7Zn, Sn-7Zn-2.5In, and Sn-7Zn-0.1Fe-0.1Co solder alloys. The XRD profiles of the Sn-7Zn alloy (Fig. 1a) show the phases of the eutectic structure, which primarily consist of several peaks indicating β-Sn (a body-center tetragonal) phases in addition to a secondary phase of hexagonal Zn IMC. The Sn-Zn phase diagram displayed in Fig. 2a shows that the low solubility of Zn in Sn of about 0.4 wt.% at 180 °C leads to the precipitation of the Zn phase as an individual phase that impedes the formation of any IMCs via the solidification process. In the case of adding 2.5 wt. % indium to Sn–7Zn alloy (Fig. 1b), XRD pattern showed the formation of γ-InSn4 IMC as new phase in addition to the originally formed β-Sn and α-Zn phases. These results indicate that during the melting process, In is efficaciously alloyed with Sn, which is in agreement with the Sn–Zn–In ternary phase diagram shown in Fig. 2b [18]. Similar data were gained by Han et al. [19]. While, the XRD analysis of the Fe/Co alloy, as shown in Figure 1c, demonstrated the creation of the following intermetallic compounds (IMCs); α-Zn, β-Sn, α-Fe, γ-Zn$_{21}$Co$_5$, γ-Co$_2$Sn$_2$Zn, and α-Fe$_{0.92}$Sn$_{0.08}$. As is widely known, Zn has a negligible solid solubility in Sn matrix. However, the addition of Fe/Co into the Sn-7Zn has improved the solubility of Zn phase in the Sn matrix. Similar data were acquired by Giefers and Nicol [20] and Li et al. [21].

3.2 Solidification microstructure of Sn-7Zn fusible alloy

As shown in Fig. 3a, the microstructure of Sn-7Zn alloy contains two phases: (i) needle-like Zn-rich intermetallic phases, represented as irregular of misaligned Zn particles, and (ii) β-Sn phase in the
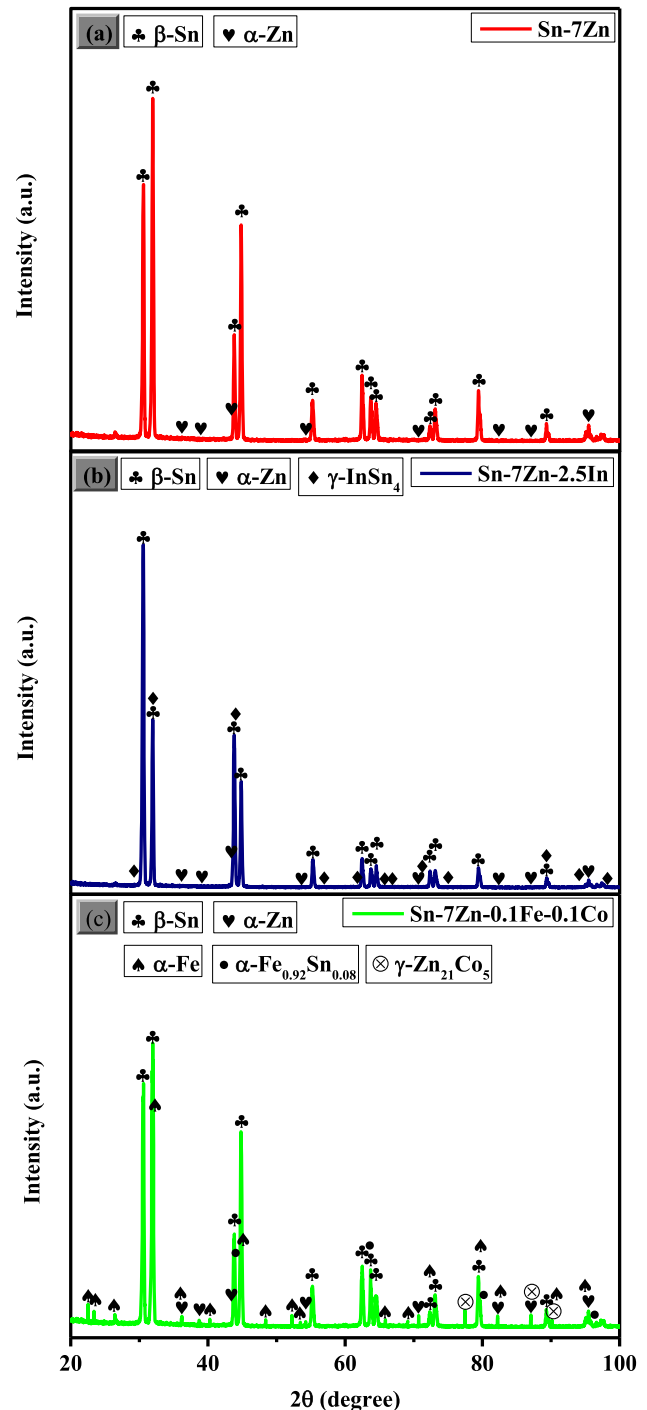
Fig. 1 XRD analysis of as-solidified **a** Sn–7Zn, **b** Sn–7Zn-2.5In and **c** Sn–7Zn0.1Fe-0.1Co solder alloys

eutectic matrix. By adding 2.5 wt.% indium, a refined microstructure is observed; notably, the Zn-rich intermetallic was homogeneously distributed and a small granular dark phase of InSn$_4$ was formed, as shown in Fig. 3b. The InSn$_4$ intermetallic has a strengthening mechanism which may act as new
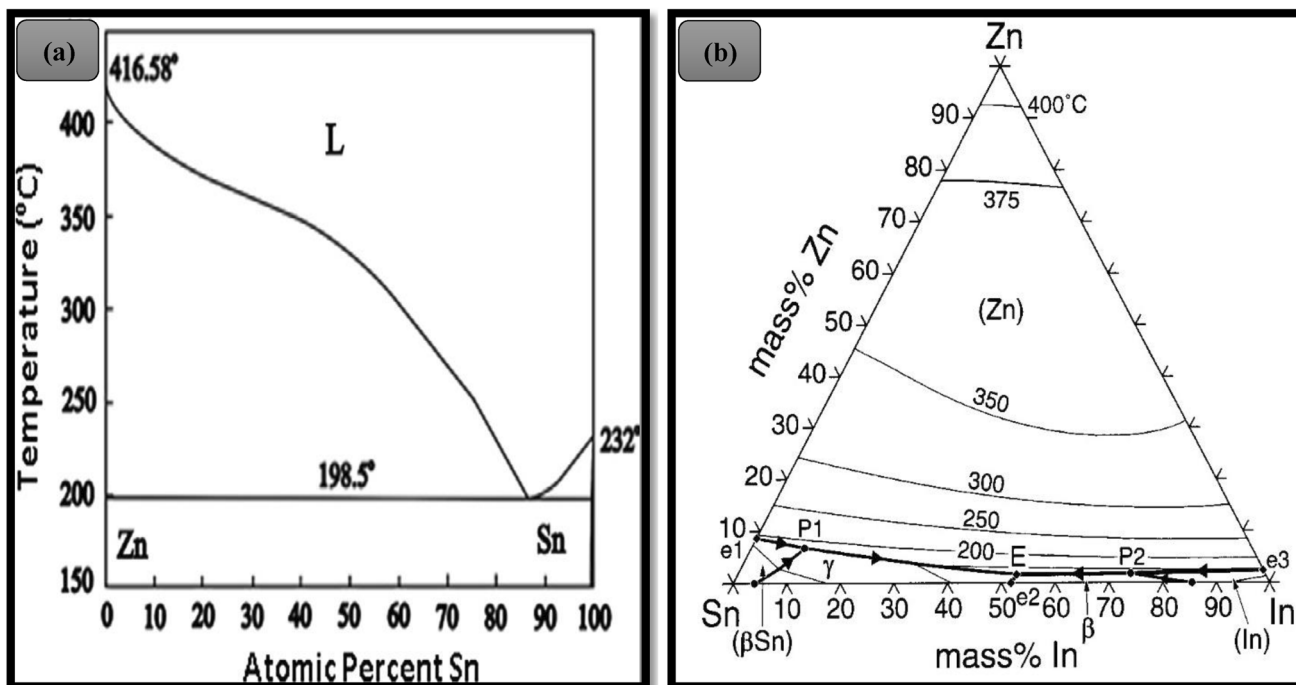
Fig. 2 **a** Binary Sn–Zn and **b** Sn–Zn–In ternary phase diagrams [7, 13]

nucleation centers to refine the microstructure within the matrix and thus enhance the mechanical characteristics of Sn–Zn-based solder. However, the addition of 0.1%Fe and 0.1%Co to the Sn-7Zn alloy as illustrated in Fig. 3c results in a finer α-Zn phase with many coarse IMCs butterfly morphology which contains α-Fe, γ-$Zn_{21}Co_5$, γ-Co_2Sn_2Zn, and α-$Fe_{0.92}Sn_{0.08}$. precipitates. These results are consistent with the XRD results. The SEM and its elemental mapping for Sn-7Zn alloy indicate that the eutectic structure is formed by Sn and Zn while the other part exists as a dark, needle-like Zn-rich phase as shown in Fig. 4a–f. On the other hand, the microstructure and EPMA elemental mapping of the Sn-7Zn-2.5In alloy are shown in Fig. 5a–f and reveal that Sn is uniformly distributed in the alloy as small dots, Zn exists as dark needle-like, and indium is distributed in bulk with an obvious round shape. Figure 6a–f shows SEM micrograph and its EPMA of the Sn–7Zn-0.1Fe-0.1Co solder alloy. The results indicate that the addition of a small amount of Fe/Co (0.1 wt.%) could decrease the agglomeration of the Zn-rich phases in solder alloy and lead to the aggregation of γ-$Zn_{21}Co_5$, γ-Co_2Sn_2Zn, and α-$Fe_{0.92}Sn_{0.08}$ phases, and Sn is distributed uniformly in the matrix as a point shape. However, from the SEM images shown in Figs. 4, 5, and 6, it is also verified that the eutectic region consists of α-Zn and β-Sn binary phases. Since the solder

alloys are often subjected to the nitric acid during etching process, the Zn-rich areas are seen to form dark needle-like grooves owing to the solubility of Zn in nitric acid. Therefore, it is expected that EPMA elemental mapping of Zn in Figs. 4, 5, and 6 not appeared as a separate phase, but appeared as uniformly distributed in Sn matrix. We will discuss the formation of these IMCs and their impact on the structural and mechanical characteristics of Sn-0.7Zn alloy. In the case of indium addition, it is uniformly dissolved in the solder and participates to form the InSn4 IMCs. Such dissolution may cause notable modifications in the lattice parameters of Zn and Sn and consequently rise in the solution's entropy [22]. The increases in the solution's entropy in turn reduce the interfacial energy of Zn liquid and support constitutional undercooling to improve inoculation [23], which is most potentially the cause of the creation of finer and more uniform Zn-rich precipitates by the addition of indium element. On the other hand, it can be said that the presence of γ-$InSn_4$ inhibits the formation of the coarsening of Zn-rich precipitates by promoting the higher nucleation density of solid phases during solidification [24]. The coarse Zn-rich phase in Sn–Zn alloy is well recognized to be averse to the mechanical dependability of the joints due to the accumulation of additional defects (e.g., dislocation) and thus increases
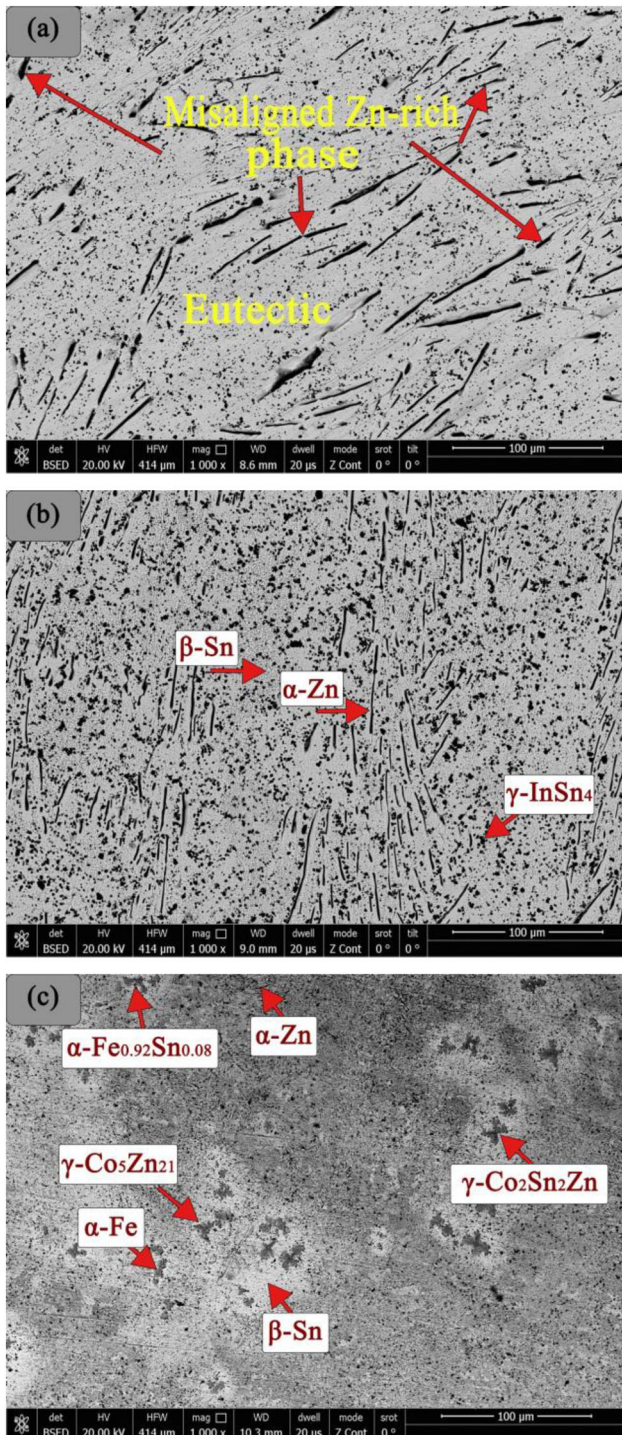
Fig. 3 Low magnification SEM image of **a** Sn-7Zn **b** Sn-7Zn-2.5In and **c** Sn-7Zn-0.1Fe-0.1Co solder alloys

susceptibility to void production [25, 26]. According to this point of view, the fine Zn phase in the Sn–Zn–In alloy could be useful for its mechanical reliability. It should also be predictable that fine and homogeneous distributed Zn-rich IMCs are helpful to the

enhancement of corrosion resistance of the solder alloy. However, the addition of Fe and Co has robust effect on both the solder microstructure and the formation of new IMCs. The 0.1% Co-doped solder alloy showed that the large needle-like α-Zn morphology was remarkably suppressed and markedly changed to fine needle-like Zn-rich phase. In addition, coarser new type of butterfly morphology which contains γ-$Zn_{21}Co_5$ and γ-Co_2Sn_2Zn precipitates was detected. The finer needle-like α-Zn precipitate can reduce the chance of propagation or crack formation, leading to circumvention of the brittleness of the solder joint. Therefore, the existence of fine needle-like α-Zn precipitate can be explained by the fact that Zn atoms of the α-Zn phase is depleted from the matrix due to the formation of γ-$Zn_{21}Co_5$ and γ-Co_2Sn_2Zn IMCs and thus, the adverse effect of Zn is further reduced. The 0.1 wt.% Fe addition to the Sn-7Zn solder led to the formation of large α-$Fe_{0.92}Sn_{0.08}$ IMC particles. These large Fe-Sn IMCs particles are sparsely distributed in the microstructure located in the eutectic regions besides the γ-$Zn_{21}Co_5$ and γ-Co_2Sn_2Zn IMC particles. It is well known that Fe has little solubility in the β-Sn matrix (and vice versa) below 200 °C. Consequently, most of the Fe precipitates as the $Fe_{0.92}Sn_{0.08}$ phase or other form, such as pure α-Fe in the eutectic regions [27]. However, in the present work, both the α-Fe and $Fe_{0.92}Sn_{0.08}$ phases were identified. Thus, the formation of fine needle-like α-Zn precipitate and large γ-$Zn_{21}Co_5$, γ-Co_2Sn_2Zn, $Fe_{0.92}Sn_{0.08}$ IMCs particles during solidification is anticipated to the higher ductility and hence the absence of micro-cracks in as-solidified state of Fe/Co bearing Sn-7Zn alloys.

3.3 Thermal behavior

Maintaining higher electronic packaging quality requires considering decisive factors such as undercooling process and the melting temperature of the solder alloys. Therefore, DSC analysis was achieved at 10 °C/min for the three solder alloys to provide information about the effects of In, Co, and Fe microalloying on the thermal characteristics of Sn-7Zn solder, and the obtained data are presented in Fig. 7 and recorded in Table 1. Results display the existence of just one endothermal peak (T_m) arising at 200.4 °C, 196.1 °C, and 202.2 °C for Sn-7Zn, Sn-7Zn-2.5In, and Sn-7Zn-0.1Fe-0.1Co alloys, respectively. On the other hand, two exothermal peaks were detected for the three samples at 194.7 and 200.9 °C
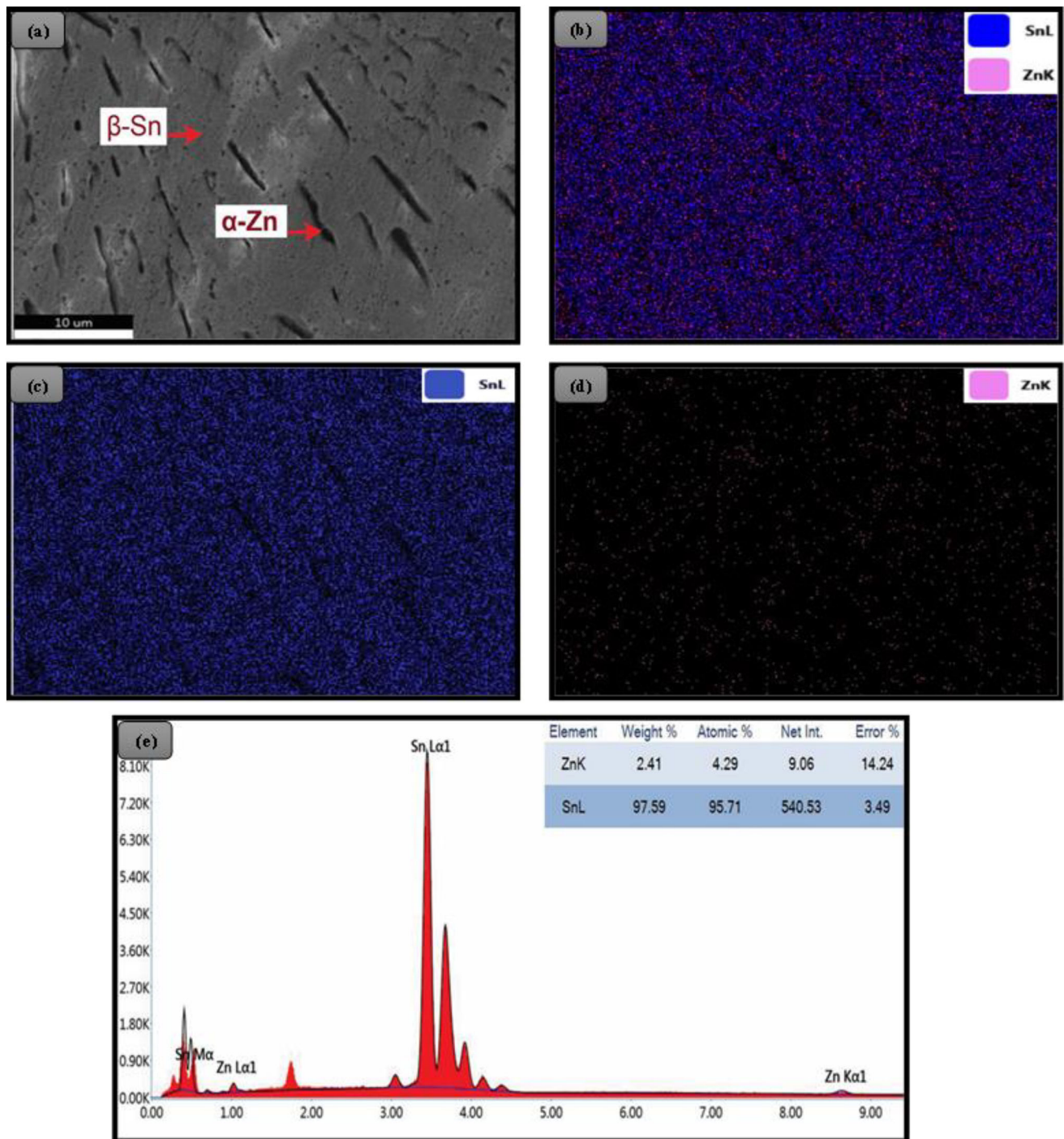
Fig. 4 High-magnification SEM microstructure of Sn–7Zn alloy and corresponding EPMA elemental mappings of Sn and Zn, showing the microstructure of β-Sn and α-Zn

for Sn-7Zn, 190.2, and 194.1 °C for Sn-7Zn-2.5In, and 194.6 and 199.1 °C for Sn-7Zn-0.1Fe-0.1Co, which exhibit a decisive reliance of T_m on the type and the quantity of addition. These results comply with that noted by El-Daly et al. [16]. Also, In Fig. 7, the intersection point method was employed to determine the solidus (T_{on}) and liquidus (T_{end}) temperatures of the examinedsolder alloys during the heating process. The difference between the liquidus temperature (T_{end}) and solidus temperature (T_{onset}) during heating is known as the pasty range, which is another assertive factor. The pasty range of eutectic
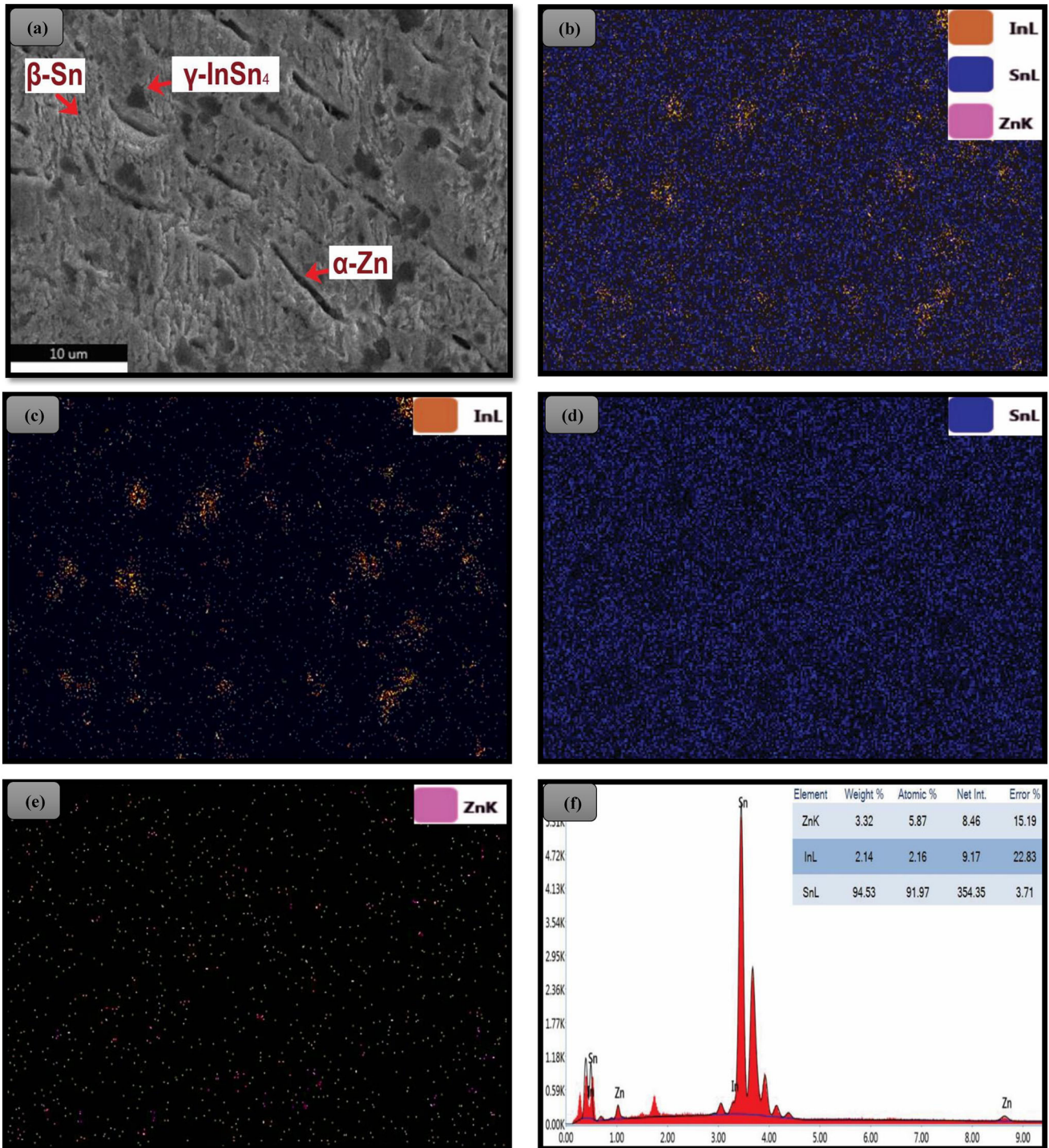
Fig. 5 High-magnification SEM microstructure of Sn–7Zn-2.5In alloy and corresponding EPMA elemental mappings of Sn, Zn and In, showing the microstructure of β-Sn, α-Zn, and, γ-InSn4

Sn–Pb solder is typically around 11.5 °C. This is a specific temperature range during the solidification process where the material is in a semi-solid state, neither fully solid nor fully liquid. Understanding this specific value is important because it can affect the quality of the final product, particularly in manufacturing processes. The pasty range of eutectic Sn–Pb solder is relatively high, and it is considered as one of its disadvantages. It can lead to issues such as hot tearing, fillet lifting, and porosity, especially
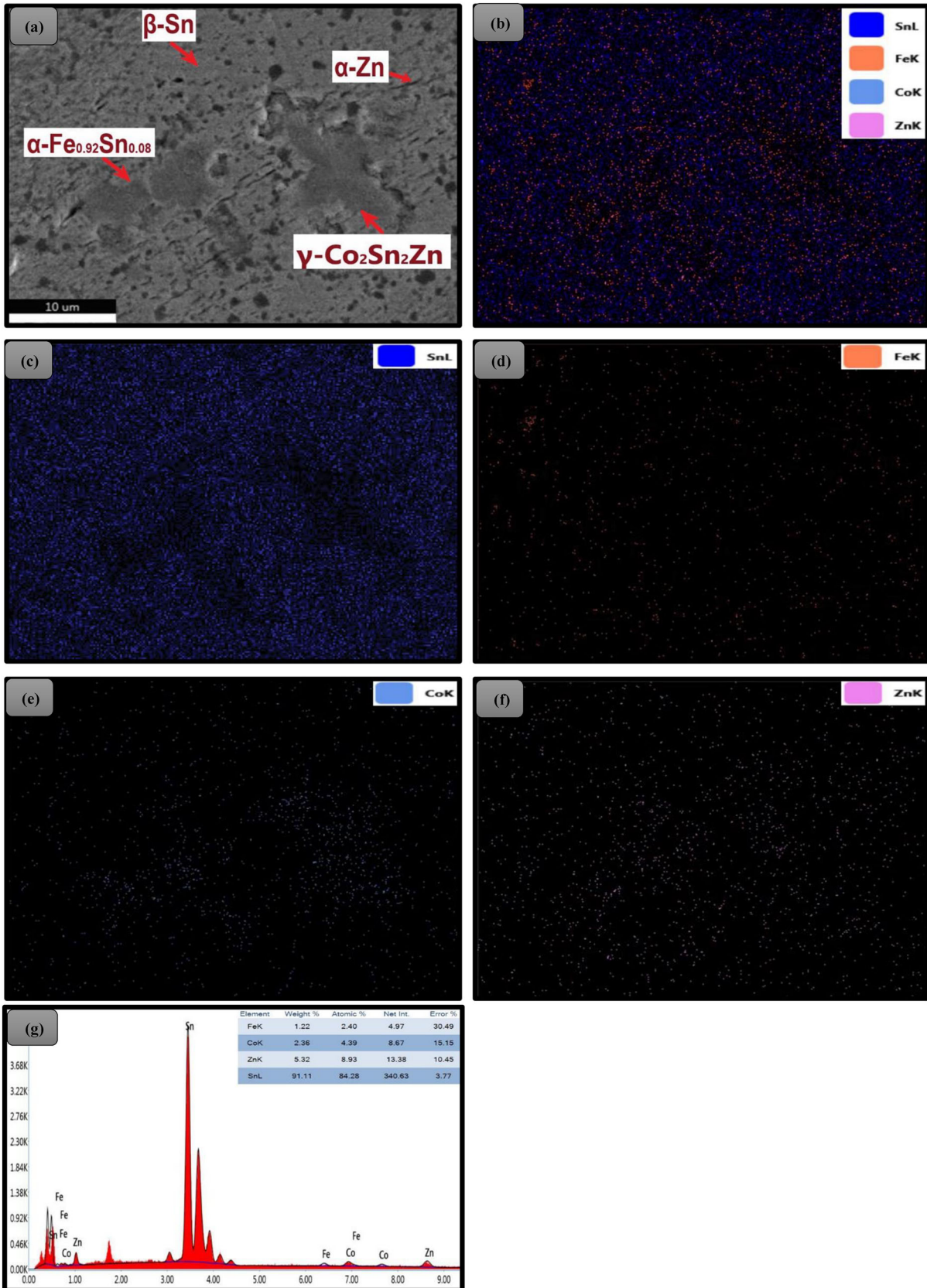
◄**Fig. 6** High-magnification SEM microstructure of Sn–7Zn-0.1-0.1Co alloy and corresponding EPMA elemental mappings of Sn, Zn, Fe, and Co, showing the microstructure of β-Sn, α-Zn, and, γ-Co2Sn2Zn
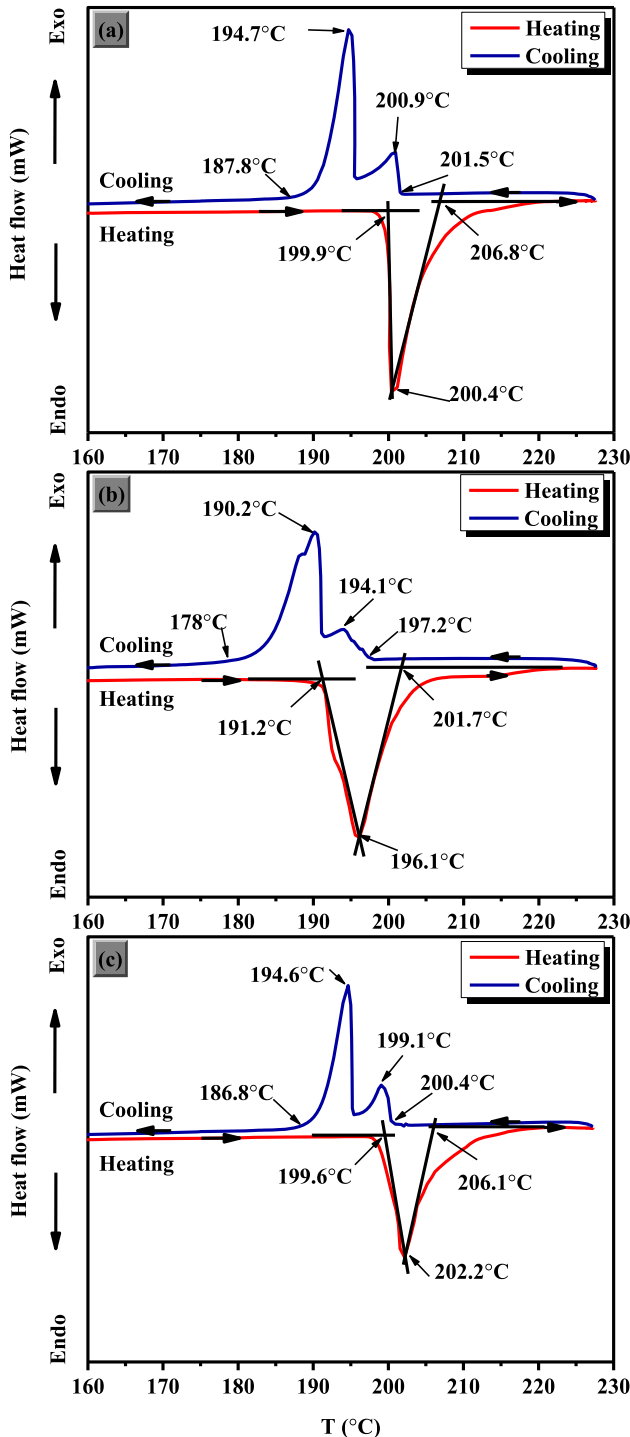

Fig. 7 DSC results of **a** Sn-7Zn, **b** Sn-7Zn-2.5In, and **c** Sn-7Zn-0.1Fe-0.1Co solder alloys during heating (endothermal) and cooling (exothermal)

when the alloy is used in microelectronics and high-reliability applications [5, 28]. The narrow pasty range means that the temperature during the solidification process needs to be controlled very precisely, which can be difficult to achieve in a manufacturing environment. It is also noted that the pasty range value obtained in this study due to the addition of In, Fe, and Co to Sn-7Zn solder alloy was lower than that of the Sn–Pb eutectic alloy, which can help to solve the aforementioned problems associated with a tin–lead alloy. In general, the addition of these elements can improve the thermal, mechanical, and microstructural properties of the solder alloy, making it more suitable for various manufacturing applications.

The undercooling value is a crucial factor in the solidification process. It can be calculated as the difference between the onset temperatures in the heating and cooling curve ($\Delta T = T_{onset}$, heating $-$ T_{onset}, cooling). Usually, the degree of undercooling is proportional to the amount of Sn in the solder. The addition of small amounts of other alloying elements to solders can lead to change undercooling, as these elements can serve as additional nucleation sites and promote solidification [29]. However, the unusual finding from DSC analysis of three alloys is the onset temperature during cooling, since it was observed to be higher than the onset temperature during heating. Accordingly, the ΔT values cannot be evaluated according to the above definition, since the variation of equilibrium solidification temperatures is caused by the change of nucleation ability of primary solidification phases of α-Zn, β-Sn, γ-InSn$_4$, γ-Zn$_{21}$Co$_5$, γ Co$_2$Sn$_2$Zn, α-Fe, and α-Fe$_{0.92}$Sn$_{0.08}$ IMCs. As an approximation, the liquidus temperature during heating was assumed to be the equilibrium solidification temperature as reported by El-Daly et al., [7]. Based on this consideration, the degree of undercooling values becomes 4.5 °C and 5.7 °C for Sn–7Zn–2.5In and Sn–7Zn–0.1Fe-0.1Co solders, respectively, as shown in Table 1. Consistent with XRD analysis shown in Fig. 1, it is assumed that addition of In or Fe and Co atoms not only substitutes at Sn and/or Zn sites to form α-Zn, β-Sn, γ-InSn$_4$, γ-Zn$_{21}$Co$_5$, γ Co$_2$Sn$_2$Zn, α-Fe, and α-Fe$_{0.92}$Sn$_{0.08}$ IMCs in the molten solder, but also precipitates during cooling to form small particles that may be considered as a primary phase. Once the solidification process begins, the degrees of undercooling can be related to the nucleation ability

Table 1 Solidus temperature (T_{onset}), liquidus temperature (T_{end}), pasty range, undercooling range, T_{onset} cooling and peak temperature during cooling, for Sn-7Zn, Sn-7Zn-2.5In, and Sn-7Zn-0.1Fe-0.1Co solder alloys

Alloy	T_{onset} heating	T_{end} heating	Pasty range (T_{end}—T_{onset})	T_{onset} cooling	Undercooling (T_{onset} heating—T_{onset} cooling)	Peak temperature
Sn-7Zn	199.9	206.8	6.9	201.5	5.3	200.4
Sn-7Zn-2.5In	191.2	201.7	10.5	197.2	4.5	196.1
Sn-7Zn-0.1Fe-0.1Co	199.6	206.1	6.5	200.4	5.7	202.2
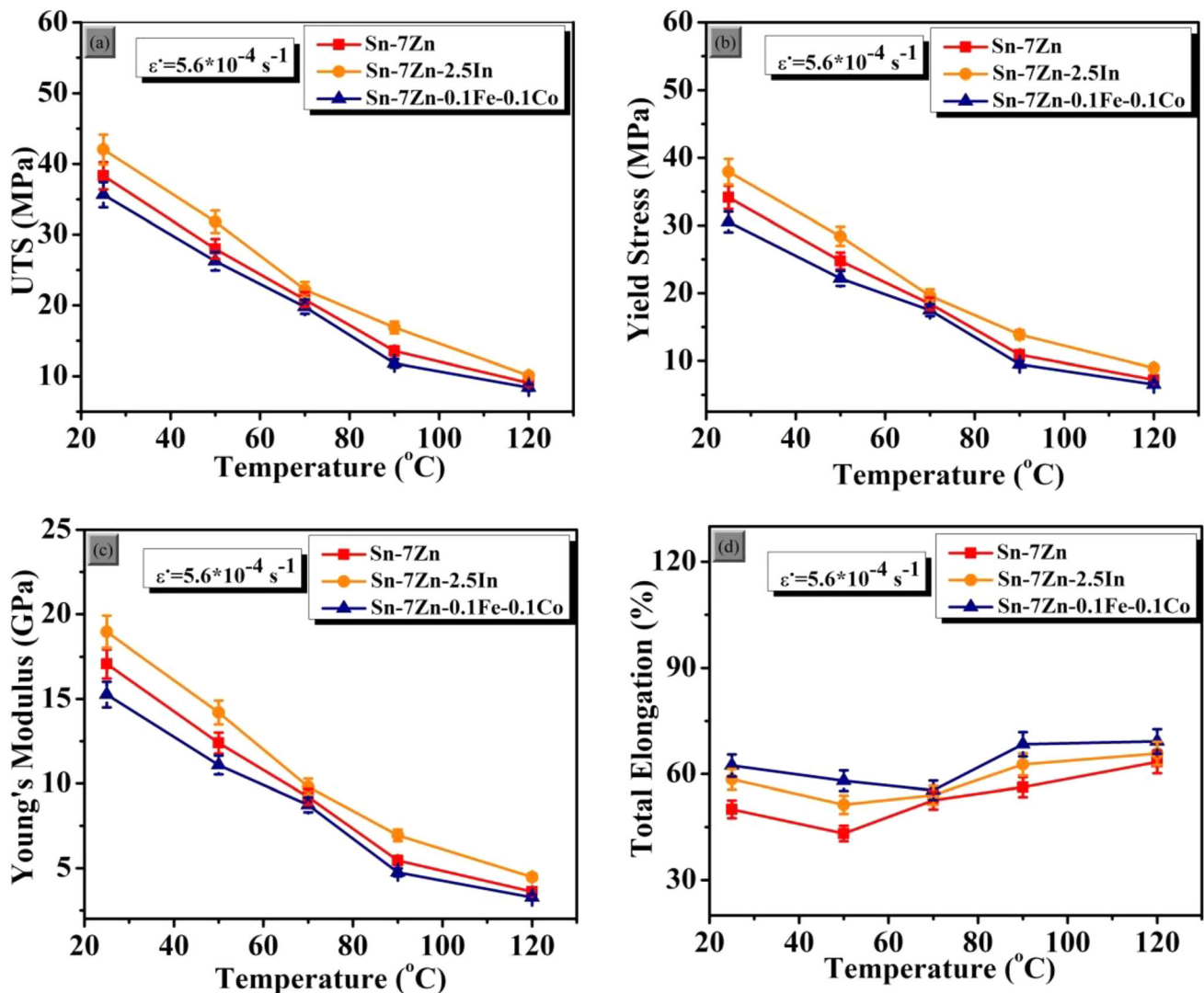
Fig. 8 Effect of temperature on **a** ultimate tensile strength (UTS), **b** yield stress (YS), **c** Young's Modulus and **d** elongation (El. %) at constant strain rate 5.6×10^4 s^{-1} and different temperatures for Sn-7Zn, Sn-7Zn-2.5In, and Sn-7Zn-0.1Fe-0.1Co alloys

of these IMCs within the melt. Nevertheless, the primary phases may not have provided the same suitable sites for heterogeneous nucleation. As a result, the degree of undercooling increases with the addition of Fe and Co while it decreases with the addition of In.
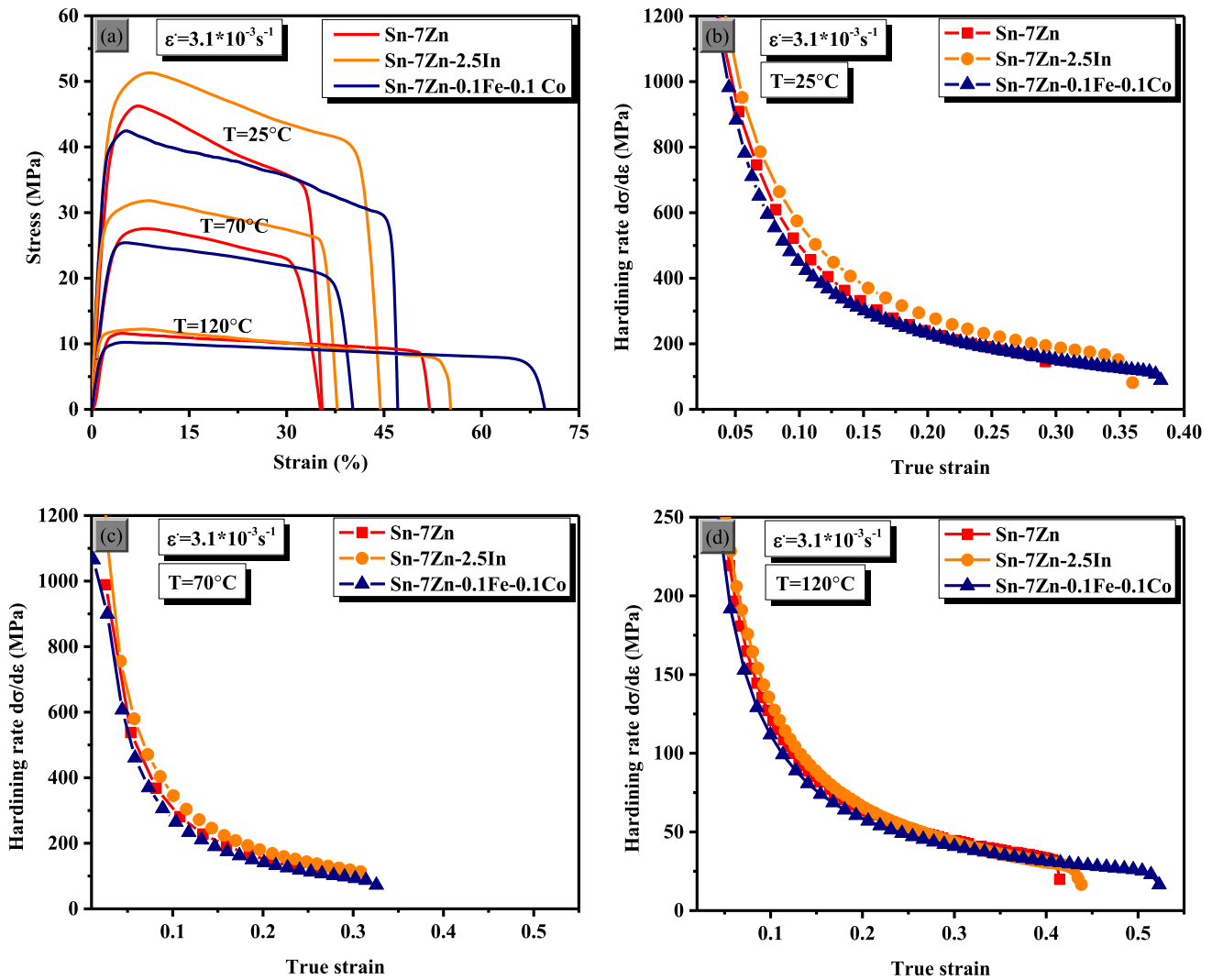
Fig. 9 Tensile properties of Sn-7Zn, Sn-7Zn-2.5In, and Sn-7Zn-0.1Fe-0.1Co alloys at different temperatures and their corresponding the work hardening response

3.4 Influence of microalloying and test temperature on the solder mechanical properties

Figures 8 and 9 illustrate the temperature influence on the tensile properties of the investigated solder alloys at a steady strain rate of 5.6×10^{-4} s^{-1} and 3.1×10^{-3} s^{-1}, respectively, while the obtained data at all the examined temperature ranges are listed in Table 2. Results revealed that the achieved stress–strain curves are liable to alloy composition. It showed that there is a continuous decrease in UTS and YS values of the investigated solders as the temperature increases, which implies that at higher temperatures and steady strain rates, the dynamic recovery process is more noteworthy. According to

these tensile tests, the Sn-7Zn solder alloy exhibited a UTS of approximately 38.3 MPa at room temperature, while microalloying with 2.5% wt.% In exhibits a higher UTS of ∼ 42 MPa. This could be ascribed to the precipitation of well-aligned fine needle-like α-Zn and enlarging the eutectic region, which may obstruct the dislocation movement. Besides, the In atoms are dissolved into the β-Sn matrix, which enhances the solid solution strengthening effect by impeding the dislocation movement that is started in the ductile β-Sn phase. On the other hand, the microalloying with 0.1% wt. Fe and 0.1% wt. Co exhibits a lower UTS of about 35.7 MPa, which could be attributable to the formation of large IMCs. Although the UTS and YS behavior are almost steady in all investigated temperature ranges, the ductility

Table 2 Mechanical property data for different solders at $\varepsilon' = 5.6 \times 10^{-4}$ s^{-1} and different temperatures

Alloy / ε	UTS (MPa)	YS (MPa)	Elongation (%)	Young's modulus (GPa)
Sn-7Zn				
25 °C	38.3	34.1	50	17.1
50 °C	28	24.8	43.2	12.4
70 °C	21	18.4	52.6	9.2
90 °C	13.6	10.9	56.3	5.5
120 °C	9.1	7.2	63.4	3.6
Sn-7Zn-2.5In				
25 °C	42	37.9	58.5	19
50 °C	31.8	28.4	51.3	14.2
70 °C	22.2	19.6	54	9.8
90 °C	16.9	13.9	62.7	6.9
120 °C	10.1	8.9	65.8	4.5
Sn-7Zn-0.1Fe-0.1Co				
25 °C	35.7	30.5	62.4	15.3
50 °C	26.3	22.8	58.1	11.1
70 °C	19.8	17.5	55.4	8.7
90 °C	11.8	9.5	68.4	4.8
120 °C	8.4	6.5	69.2	3.3

as estimated by the elongation percentage has increased and decreased in erratic patterns. But in general, we can notice that the addition of In resulted in increasing both strength and ductility of the Sn-7Zn alloy, which is a dream come true for the soldering process. Conversely, the addition of Fe and Co results in an enhancement of the ductility of Sn-7Zn solder and keeps the UTS values at approximately the same level. Figure 10b–d shows the representative hardening rate versus the true strain of the three solders. As we can see, the highest hardening rate value at 25 °C was 2.5GPa for Sn-7Zn-2.5In alloy at zero true strain, while the lowest hardening rate value was 1.7GPa for the Sn-7Zn-0.1Fe-0.1Co alloy at zero strain rate. However, these values were significantly decreased by rising the testing temperature, where the hardening rate values became 2.3GPa and 0.9GPa, respectively, at 70 °C, and 1.1GPa and 0.53GPa, respectively, at 120 °C, revealing a remarkable softening after yielding had been carried out by rising the investigated temperatures.

The comparison of ductility for three solders indicates the better performance of Sn-7Zn-0.1Fe-0.1Co alloy solder, as achieved from its higher level of elongation when considered at most temperatures and strain rate levels. These results also imply that high positive strain rate sensitivities are necessary to produce high plasticity at certain strain rate and temperature. The ductility sensitiveness to the experiment temperatures could be a result of several

possible reasons, such as stability of hard and soft IMC in solder matrix, composition of alloy, growth rate, and grain size [20]. From the tensile results, it's clear to see that, through hot deformations depending on the flow stress growth, both dynamic flow softening and work hardening have occurred. As a rule, the dislocation movement could be increased because of increasing the deformation temperature, leading to the dynamic flow softening, which is basically driven by dynamic recovery, particularly at lower strain rates, since the lower strain rates provide a sufficient time for the dynamic recovery to expend the kept and stored energy. However, the mechanical strength and ductility of Sn-Zn and Sn-Zn-Fe/Co solder alloys are influenced by several mechanisms as follows: (a) strain hardening which is a mechanism that increases the strength of a material as it is deformed. In solder alloys, strain hardening is caused by the movement and interaction of dislocations, which are defects in the crystal lattice. This mechanism is responsible for the increase in strength observed at high strains and can contribute to the overall ductility of the alloy; (b) dynamic recovery, which is the ability of the alloy to recover its original shape after being deformed. Dynamic recovery is caused by the movement and rearrangement of atoms within the crystal lattice and is influenced by the temperature and strain rate of the test. At high strain rates, it can be noted that the ductility of Sn-Zn and Sn-Zn-Fe/Co solder alloys is influenced by
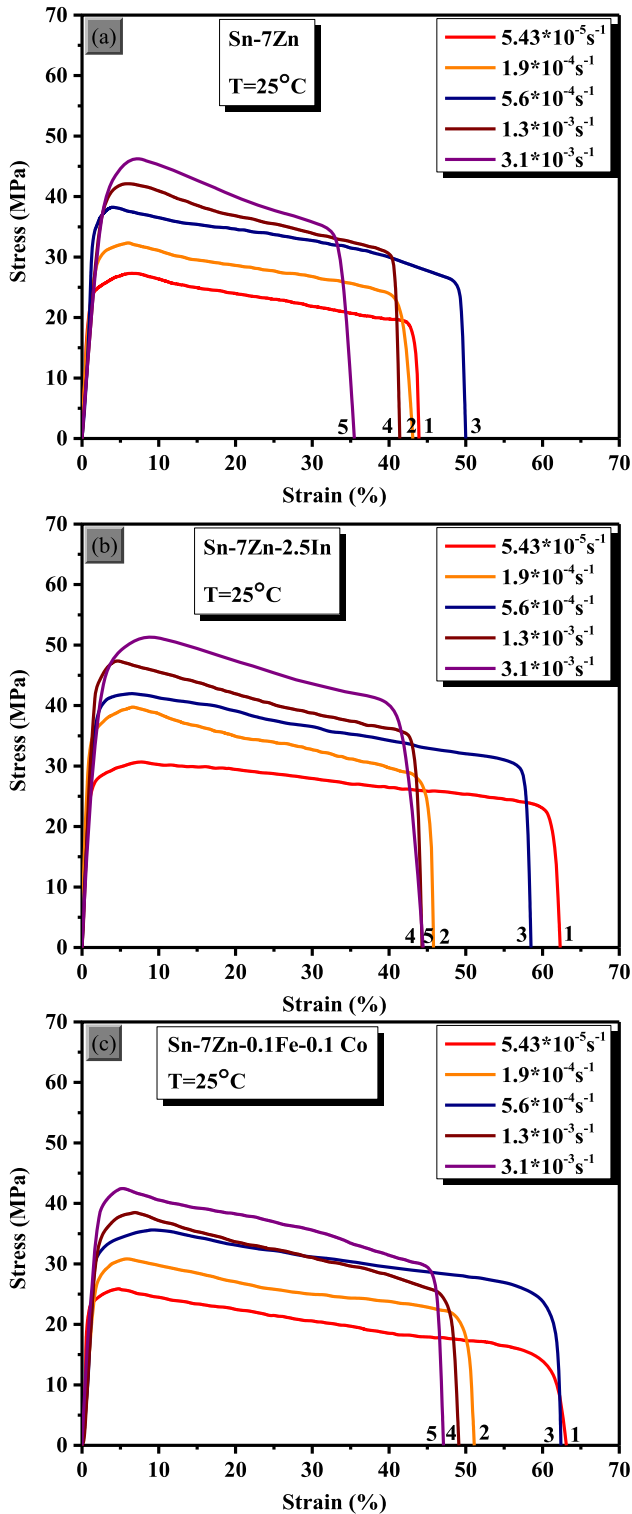
Fig.10 Tensile properties of **a** Sn-7Zn, **b** Sn-7Zn-2.5In and **c** Sn-7Zn-0.1Fe-0.1Co solder alloys at different strain rates at 25 °C

where the grains within the alloy slide past each other. This can help to reduce the stress within the grains and can contribute to the overall ductility of the alloy; and (d) intermetallic, such as γ-$Zn_{21}Co_5$, γ-Co_2Sn_2Zn, and α-$Fe_{0.92}Sn_{0.08}$ in solder alloys, can have a significant effect on their mechanical properties. IMCs can act as sites for dislocation nucleation and can also act as barriers to dislocation motion, which can influence the ductility of the alloy. In Sn–Zn–Fe/Co solder alloys, Fe and Co are added as a strengthening element, which can form IMCs with Sn and Zn. These IMCs can act as obstacles for dislocations and affect the ductility of the alloy. It is important to note that these mechanisms interact with each other, and the overall ductility of the alloy is a balance of these mechanisms and their interplay.

3.5 Influence of strain rate on the mechanical properties of solder alloys

Typical stress–strain behavior of the Sn-7Zn, Sn-7Zn-2.5In, and Sn-7Zn-0.1Fe-0.1Co alloys at constant temperatures of 25 °C with a changing strain rate from 5.43×10^{-5} to 3.1×10^{-3} s^{-1} are displayed in Fig. 10. The obtained data revealed that the increase in strain rate from 5.43×10^{-5} to 3.1×10^{-3} s^{-1} led to an increase in the UTS of the alloys, which reveals a significant reliance of UTS on the strain rate. UTS values show an increase from 27.3 to 46.6 MPa for the Sn-7Zn alloy. The addition of 2.5 wt.% In leads to an increase of the UTS from 30.7 to 51.5 MPa (with an average increase of $\sim$ 12% when comparing to the base Sn-7Zn). The addition of 0.1 wt.% Fe and 0.1 wt.% Co led to an increase in UTS values from 26 to 42.6 MPa (with an average decrease of about $\sim$ 7% when comparing to the base Sn-7Zn). However, the results revealed a random increase in elongation values as the strain rate increases, which indicates a small effect of strain rate on the ductility of samples in the examined strain rate ranges. The results display that doping of 2.5 wt.% In into the Sn-7Zn system leads to an enhancement in both UTS " $\sim$ 1.1 times that of the binary Sn-7Zn" and elongation "ductility" from $\sim$ 1.1 to $\sim$ 1.4 times that of the binary Sn-7Zn," which offers a robust sign that In-microalloying has an enormous effect on both tensile performance and deformation mechanisms. That means the Sn-7Zn-2.5In alloy possessed a viscoelastic property. Similar data were obtained by El-Daly et al.

dynamic recovery; (c) grain boundary sliding (GBS) is a mechanism that occurs during deformation,
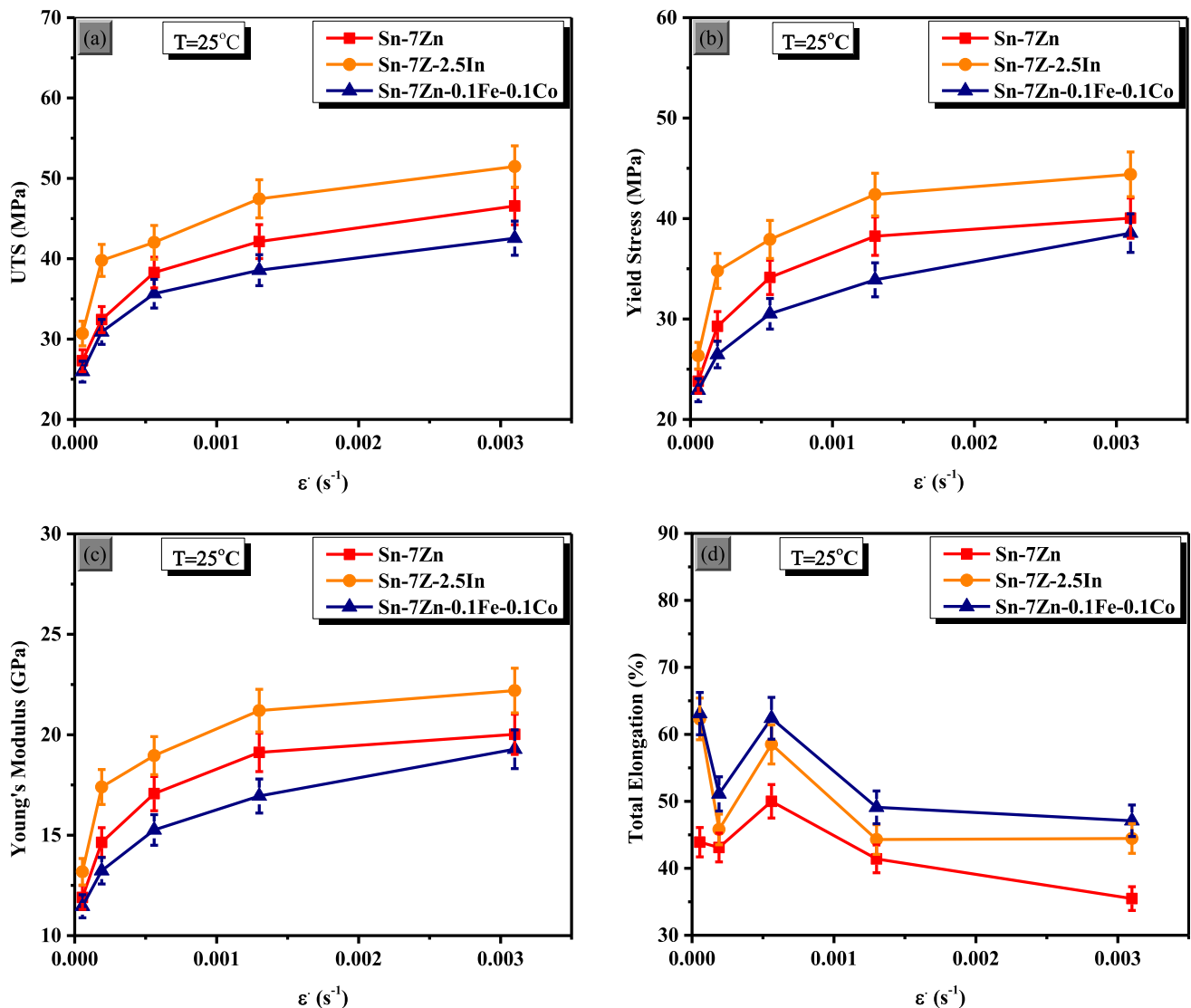
Fig.11 Effect of strain rate on **a** ultimate tensile strength (UTS), **b** yield stress (YS), **c** Young's Modulus and **d** elongation (El. %) at T = 25 °C for Sn-7Zn, Sn-7Zn-2.5In, and Sn-7Zn-0.1Fe-0.1Co alloys

[30]. These results could be attributed to the formation of γ-InSn$_4$ IMC. On the other hand, the microalloying of 0.1%wt Fe and 0.1 wt.% Co to the Sn-7Zn system results in the formation of coarse IMCs as discussed earlier. This coarsening IMCs formation is reflected in the tensile properties of the quaternary alloy by decreasing the UTS "from 0.8 to 0.9 times that of the binary Sn-7Zn" and increasing the elongation "from ~ 1.1 to ~ 1.4 times that of the binary Sn-7Zn." The influence of UTS, YS, Young's modulus, and the elongation at temperatures on strain rate at 25 °C for the three solder alloys is shown in Fig. 11. The present results compared to results from a previous study are summarized in Table 3 [13].

3.6 Constitutive equations "kinetic analysis of solders during hot deformation"

Stress exponent (*n*) and activation energy (*Q*) are crucial thermodynamic and mechanical parameters that are usually utilized to determine the tensile deformation mechanism. To establish the association between the minimum creep rate and the applied stress, we can use the following power-law relation [31]

Table 3 Mechanical property data for different solders at temperatures 25 oC, 70 oC and 120 °C and various strain rates

Solder/strain rate	25 °C			70 °C			120 °C		
	UTS (MPa)	Ys (MPa)	El	UTS (MPa)	Ys (MPa)	El	UTS (MPa)	Ys (MPa)	El
Sn-7Zn									
5.43×10^{-5} s^{-1}	27.3	23.8	43.9	13.1	10.2	67.8	6.2	5	73.9
1.9×10^{-4} s^{-1}	32.4	29.3	43.1	16.2	14.4	54.2	7.2	5.8	69.5
5.6×10^{-4} s^{-1}	38.3	34.1	50	20.8	18.4	52.6	9.1	7.2	63.4
1.3×10^{-3} s^{-1}	42.1	38.2	41.4	24.7	22.5	40.3	9.8	9.1	54.8
3.1×10^{-3} s^{-1}	46.6	40	35.5	27.7	25	35.2	11.6	10.9	52
Sn-7Zn-2.5In									
5.43×10^{-5} s^{-1}	30.7	26.4	62.3	14.3	12.5	77.2	7	5.7	80.5
1.9×10^{-4} s^{-1}	39.8	34.8	45.8	18.2	15.7	59.2	8.6	7.9	75.6
5.6×10^{-4} s^{-1}	42	37.9	58.5	22.2	19.6	54	10.1	8.9	65.8
1.3×10^{-3} s^{-1}	47.5	42.4	44.3	26.7	25.1	44.1	11.3	10.3	58.2
3.1×10^{-3} s^{-1}	51.5	44.4	44.5	31.9	28.5	37.8	12.2	11.3	55.3
Sn-7Zn-0.1Fe-0.1Co									
5.43×10^{-5} s^{-1}	26	22.9	63.1	11.3	9.1	79.1	5	3.4	84.3
1.9×10^{-4} s^{-1}	30.9	26.5	51.1	14.9	12.7	61.9	6.8	5.4	77.5
5.6×10^{-4} s^{-1}	35.7	30.5	62.4	19.8	17.5	55.4	8.4	6.5	69.2
1.3×10^{-3} s^{-1}	38.6	33.9	49.1	23.1	20.9	55.8	8.9	7.8	60
3.1×10^{-3} s^{-1}	42.6	38.6	47.1	25.6	22.7	40.2	10.2	9.1	69.8
Sn-6.5Zn-0.5Cu [7]									
5.0×10^{-5} s^{-1}	22.9	20.6	59	14.1	13.4	84.0	–	–	–
3.3×10^{-4} s^{-1}	28.4	24.2	40	18.9	17.1	71.1	–	–	–
5.4×10^{-4} s^{-1}	29.6	26.5	58.4	21.1	18.3	65.3	–	–	–
1.15×10^{-3} s^{-1}	39.0	34.8	50.7	27.2	25.2	49.8	–	–	–
2.9×10^{-3} s^{-1}	44.6	38.7	43.7	32.1	27.9	29.5	–	–	–

$$\dot{\varepsilon} = A\sigma^n exp(-Q/RT) \qquad (1)$$

The Garofalo hyperbolic sine law described below shows that the UTS is usually regarding to the homologous temperatures and strain rate, which is fitting for the constitutive analysis over wide ranges of deformation;

$$\dot{\varepsilon} = A[\sinh(\alpha\sigma)]^n exp\{\frac{-Q}{RT}\} \qquad (2)$$

where A is the material-dependent constant, α is the stress coefficient and has the units of (MPa^{-1}), σ is the applied stress and has the units of (MPa), n is the stress exponent constant, R is the gas constant (8.314 Jol^{-1} K^{-1}), T is the absolute temperature and has the units of (K), and Q is the activation energy and has the units of (kJ/mol) [16].

Taking the natural logarithm of Eq. (2):

$$ln\dot{\varepsilon} = lnA + nln[sinh(\alpha\sigma)] - Q/RT \qquad (3)$$

The value of stress coefficient (α) was calculated by $\alpha = \beta/n_1$, where β and n_1 are, respectively, the

average slopes of $ln(\dot{\varepsilon}) - \sigma$ lines and $ln(\dot{\varepsilon}) - ln(\sigma)$ lines at constant T, as shown in Fig. 12. The slope of $ln(\dot{\varepsilon})$ against ln [sinh ($\alpha\sigma$)] plot then gave the value of n (Fig. 13). The value of ln(A) could then be obtained from the intercept of the $ln(\dot{\varepsilon})$ against ln [sinh ($\alpha\sigma$)] plot. To explain the mechanism of tensile deformation, it is worth noting that three distinct mechanisms could potentially occur during the process: grain boundary sliding, which occurs when $n = 1–2$, grain boundary diffusion, which occurs when $n = 3$, and dislocation climb, which occurs when $n = 4–8$ [32, 33].

As shown, the data listed in Table 4 reveals that the values of n are between 4.24 and 6.31 for the investigated samples, which means that the tensile deformation mechanism is dislocation climb. On the other hand, it is found that n-values decreased as the temperature increased, which may be attributed to the morphology instability that occurs at high deformation temperatures [34]. In addition, as shown in Fig. 14, the relationship between ln (ε) and 1/T could be used to estimate the activation energy
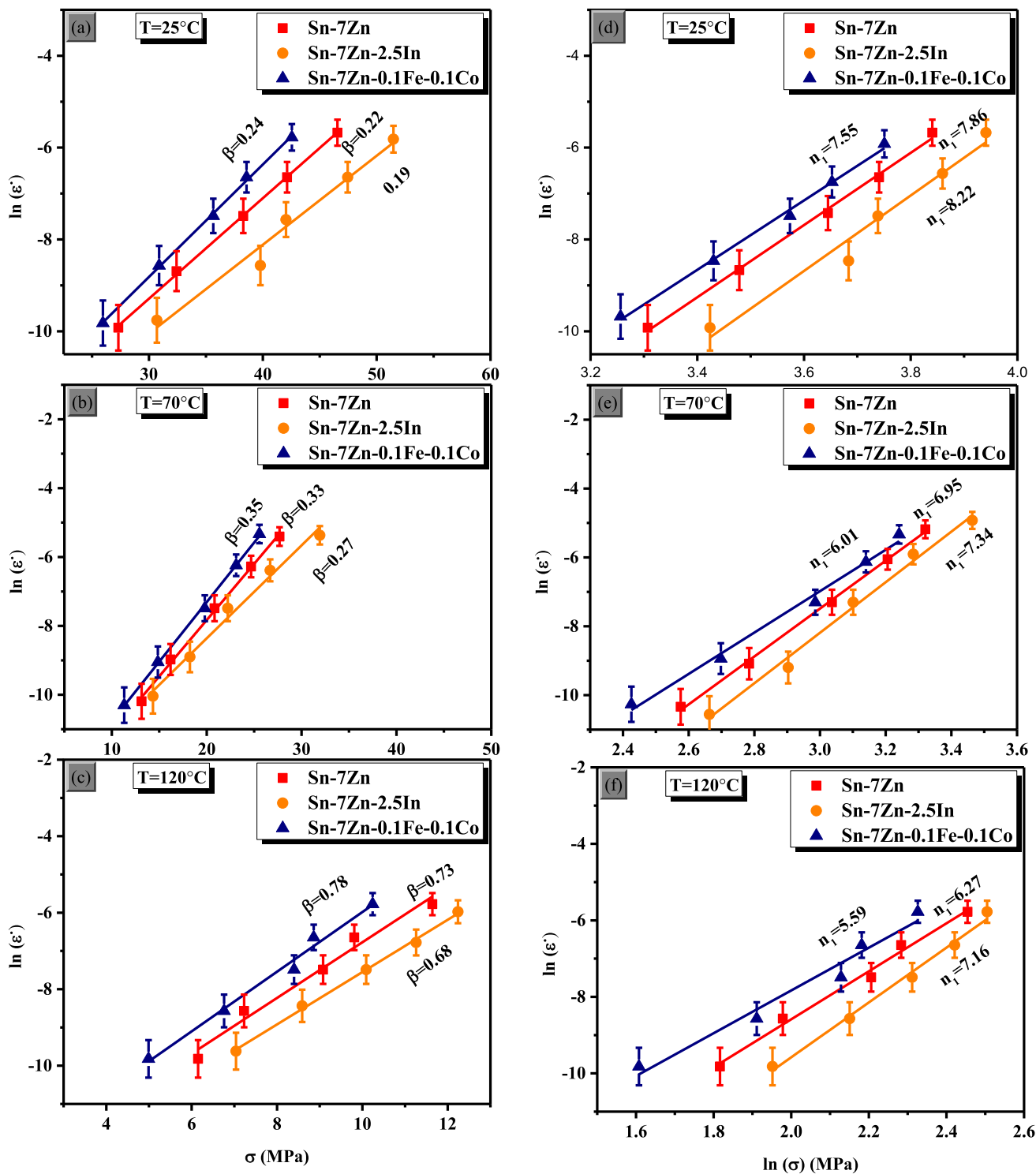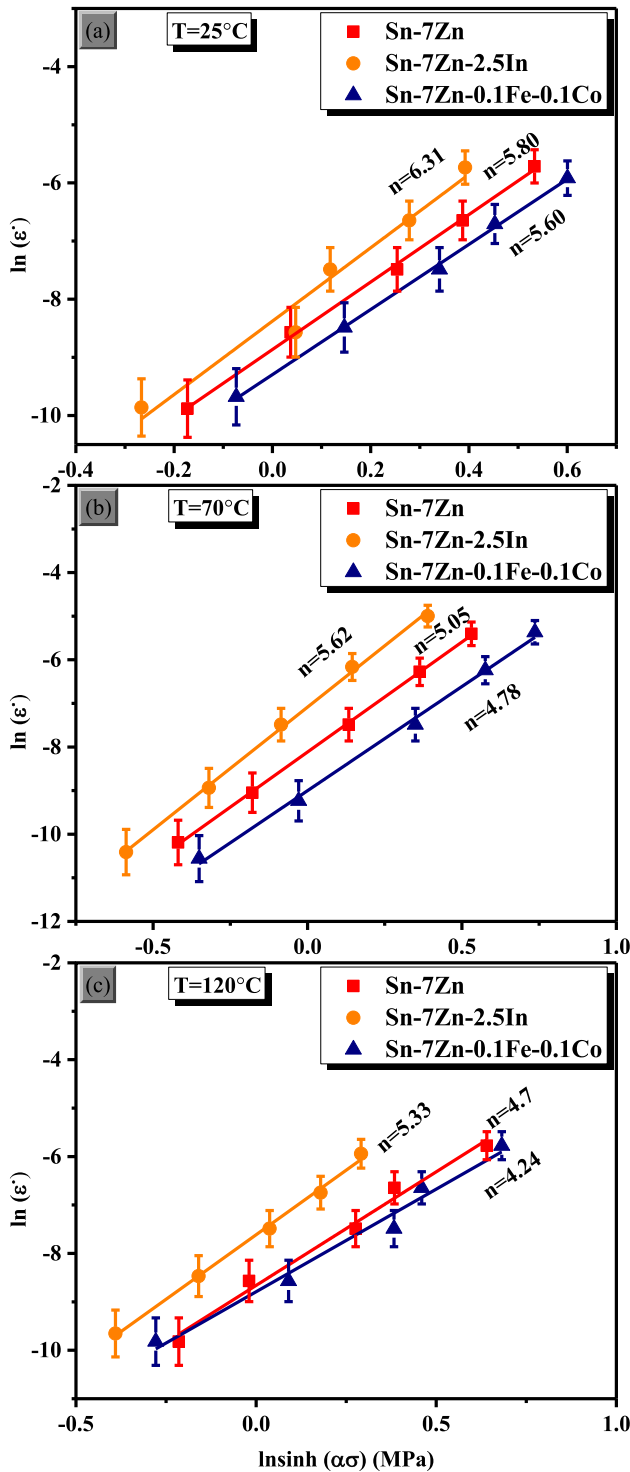
Fig.12 Relationship between σ and ln(ε.) and between ln(σ) and ln(ε.) at T = 25 °C, T = 70 °C and 120 °C for Sn-7Zn, Sn-7Zn-2.5In, and Sn-7Zn-0.1Fe-0.1Co solder alloys

(Q) value in the temperature range of 25–120 °C, with the results listed in Table 4. The Q values were found to be 78.8 kJ/mol for the Sn-7Zn alloy, 84.6 kJ/mol for the Sn-7Zn-2.5In, and 75.9 kJ/mol for the Sn-7Zn-0.1Fe-0.1Co, which indicates that the deformation mechanism for the three investigated solders is

Fig.13 Relationship between ln sinh (ασ) and ln(ε.) at T = 25 °C, T = 70 °C and 120 °C for Sn-7Zn, Sn-7Zn-2.5In, and Sn-7Zn-0.1Fe-0.1Co solder alloys

controlled by a lattice self-diffusion mechanism [35]. On the other hand, exponential type equations could be used as a model to reveal the effects that occurred on the deformation process owing to the common influence of temperature and strain rate on it. Nevertheless, the assembled results of A, Q, n, and α for the investigated solders were fitted with the Garofalo hyperbolic sine law as follows:

$$\dot{\varepsilon}_1 = 2.99 * 10^{-4}[\sinh(0.047\sigma)]^{5.05}\exp\left\{\frac{-78.8}{RT}\right\} \quad (4)$$

$$\dot{\varepsilon}_2 = 8.37 * 10^{-4}[\sinh(0.037\sigma)]^{5.62}\exp\left\{\frac{-84.6}{RT}\right\} \quad (5)$$

$$\dot{\varepsilon}_1 = 1.23 * 10^{-4}[\sinh(0.058\sigma)]^{4.78}\exp\left\{\frac{-75.9}{RT}\right\} \quad (6)$$

The data obtained through the Eqs. 4, 5, and 6 could be used to plot a comparison between the experimental data for stress vs. strain rate behavior and the Garofalo model at 70 °C as shown in Fig. 15, which exhibits excellent relevance between theoretical and experimental stress vs strain rate data at all strain rates up to approximately 2×10^{-3} s^{-1} and stresses up to 22–25 MPa. However, a slight deviation at higher stresses and strain rates has been observed for the three solder alloys. Some possible causes of deviation between experimental and model data include the material properties, the microstructure effects of solder alloy and strain rate sensitivity parameter $m = 1/n$. Equations 4–6 considered that the stress sensitivity parameter n is constant at all strain rates and stresses, while it changed experimentally at different strain rates and stresses according to the condition of superplasticity.
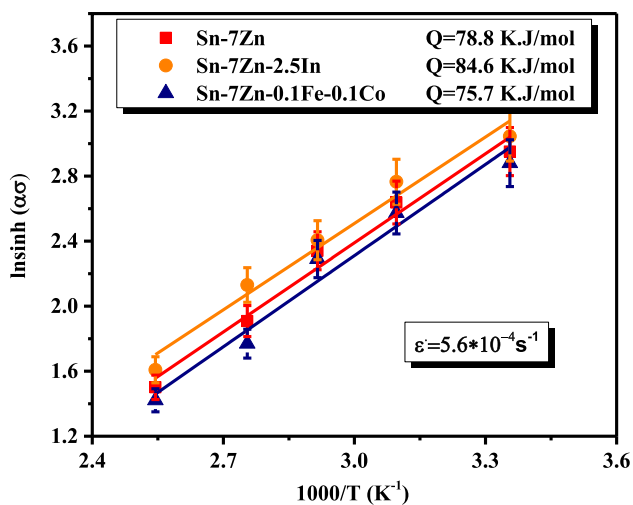
4 Conclusions

Sn–Zn alloy possess multiple fascinating features such as low cost, low melting temperature (∼ 198 °C) ,as well as satisfactory mechanical properties. In this investigation, a comparison between the microstructural formation and the thermal and mechanical characteristics of the ternary Sn-7Zn-2.5In and quaternary Sn-7Zn-0.1Fe-0.1Co solder alloys was made to find out the extent of the effect of distinct microalloying of In and dual Fe/Co on the characteristics of the binary Sn-7Zn solder alloy. The most significant data are listed as follows:-

1) Microstructural modifications were observed with the microalloying of 2.5 wt.% In to the binary Sn-7Zn solder alloy, e.g., the forming of the new

Table 4 The activation energy (Q) and stress exponent (*n*) values for Sn-7Zn, Sn-7Zn-2.5In, and Sn-7Zn-0.1Fe-0.1Co solder alloys

Alloy	Q (KJ/mol)	Temperature (°C)	α	*n*
Sn-7Zn	78.8	25	0.028	5.80
		70	0.047	5.05
		120	0.120	4.69
Sn-7Zn-2.5In	84.6	25	0.023	6.31
		70	0.037	5.62
		120	0.090	5.33
Sn-7Zn-0.1Fe-0.1Co	75.9	25	0.032	5.60
		70	0.058	4.78
		120	0.140	4.24

Fig.14 The activation energy (*Q*) values of Sn-7Zn, Sn-7Zn-2.5In, and Sn-7Zn-0.1Fe-0.1Co solder alloys
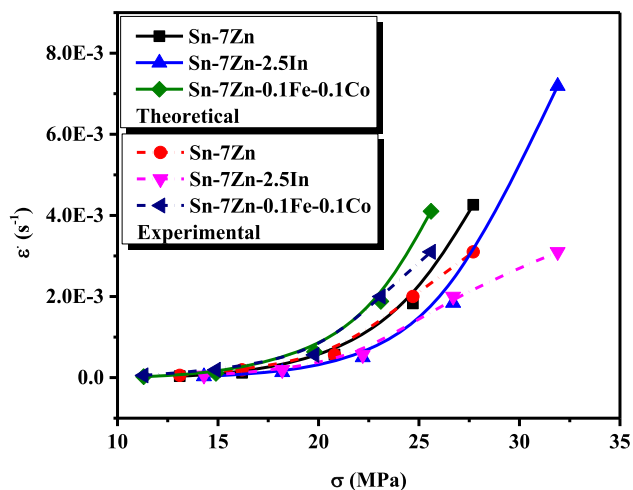
Fig.15 Comparison of strain rate achieved from experimental results and Garofalo model at 70 °C

$InSn_4$ IMC distributed in the eutectic region and the impression of needle-like α-Zn phases.

2) The minor additions of Fe and Co (0.1 wt.% for each) are tremendously modified the microstructure of the binary Sn-7Zn alloy by forming new coarsening γ-$Zn_{21}Co_5$, γ-Co_2Sn_2Zn, and α-$Fe_{0.92}Sn_{0.08}$ IMCs.

3) Thermal analysis results indicate that the addition of In decreases the degree of undercooling from 5.3 to 4.5 °C, while Fe and Co additions slightly increase it to 5.7 °C. Moreover, In or Fe and Co additions preserve the pasty range values below 11.5 °C, which allows the use of In or Fe and Co-containing Sn-7Zn alloy to be an excellent candidate in the line with different circumstances of usage, meeting the working temperature requirements of ventilation.

4) The UTS, US, and ductility of Sn-7Zn solder alloy are all improved by In microalloying. Consequently, In microalloying can improve plastic energy dissemination ability in addition to the bulk conformity of the solder interconnections, while Fe/Co-microalloying exhibit enhanced ductility in Sn-7Zn fusible solder alloy, which can be applied to the design of mitigation devices for fusible alloys.

5) The activation energies for the Sn-7Zn alloy were found to be 78.8 kJ/mol and 84.6 kJ/mol for the Sn-7Zn-2.5In, and 75.9 kJ/mol for the Sn-7Zn-0.1Fe-0.1Co, indicating that the Sn-7Zn and Sn-7Zn-0.1Fe-0.1Co deformation mechanisms are controlled by a lattice self-diffusion mechanism.

6) The Garofalo model is suitable for expressing the experimental flow behavior of Sn–7Zn solders over the examined strain rate and temperature range.

Author contributions

AME-T contributed to supervision, conceptualization, methodology, writing-review, and editing. SAM contributed to supervision, conceptualization, methodology, project administration, and review. IHL contributed to investigation, data curation, software, conceptualization, methodology, validation, and resources.

Funding

Data availability

Raw data were generated at physics department—faculty of Science—Zagazig University. Derived data supporting the findings of this study are available from the corresponding author upon request.

Declarations

Competing interests The authors declare that they have no known competing financial interests or personal relationships that could have appeared to influence the work reported in this paper.

Research involving human and/or animal participants The authors declare that this article does not contain any studies involving human participants performed by any of the authors. This article does not contain any studies involving animals performed by any of the authors.

References

1. L. Sun, L. Zhang, S.J. Zhong, J. Ma, L. Bao, J. Mater. Sci.: Mater. Elec. **26**(11), 9164 (2015)
2. A.M. El-Taher, A.F. Razzk, Met. Mater. Int. **27**, 4294 (2021)
3. A.A. El-Daly, A.Z. Mohamad, A. Fawzy, A.M. El-Taher, Mater. Sci. Eng. A **528**, 1055 (2011)
4. K. Seo, S.K. Kang, D.Y. Shih, H.M. Lee, J. Electron. Mater. **38**(2), 257 (2009)
5. A.M. El-Taher, A.A. Ibrahiem, A.F. Razzk, J. Mater. Sci.: Mater. Elec. **31**, 5521 (2020)
6. J.C. Liu, G. Zhang, Z.H. Wang, J.S. Ma, K. Suganuma, J. Mater. Des. **84**, 331 (2015)
7. A.A. El-Daly, W.M. Desoky, A.F. Saad, N.A. Mansor, E.H. Lotfy, H.M. Abd-Elmoniem, H. Hashem, J. Mater. Des. **80**, 152 (2015)
8. W. Chen, S. Xue, H. Wang, J. Wang, Z. Han, J. Mater. Sci: Mater. Elect. **21**, 496 (2010)
9. Y.H. Hu, S.B. Xue, H. Wang, H. Ye, Z.X. Xiao, L.L. Gao, J. Mater Sci: Mater. Electron **22**, 481 (2011)
10. X. Chen, M. Li, X.X. Ren, A.M. Hu, D.L. Mao, J. Electron. Mater. **35**(9), 1734 (2006)
11. M. Mccormack, S. Jin, H.S. Chen, J. Electron. Mater. **23**(7), 687 (1994)
12. J.Y. Li, J. Peng, R.C. Wang, Y. Feng, C.Q. Peng, J. Mater. Sci. (2018). https://doi.org/10.1007/s10854-018-0120-z
13. Massalski, Thaddeus B., Okamoto, H., Subramanian, P., Kacprzak, L., & Scott, W. W. (Eds.). Binary alloy phase diagrams (Vol. 1, No. 2). Metals Park, OH: American society for metals, (1986).

14. D. Yu, H. Xie, L. Wang, J. Alloy. Compd. **385**, 119 (2004)

15. S.C. Cheng, K.L. Lin, J. Elec. Mater. **31**, 940 (2002)

16. A.A. El-Daly, A.M. El-Taher, S. Gouda, J. Mater. Des. **65**, 796 (2015)

17. G. Saad, S.A. Fayek, A. Fawzy, H.N. Soliman, Gh. Mohammed, J. Mater. Sci. Eng. A **527**, 904 (2010)

18. I. Ohnuma, Y. Cui, X.J. Liu, Y. Inohana, S. Ishihara, H. Ohtani, R. Kainuma, K. Ishida, J. Elec. Mater. **29**(10), 1113 (2000)

19. D.L. Han, Y.A. Shen, S. Jin, H. Nishikawa, J. Mater. Sci. Metals Corros. **55**, 10824 (2020)

20. H. Giefers, M. Nicol, J. Alloy. Compd. **422**, 132 (2006)

21. J.S. Li, Z.J. Feng, L.J. Yuan, W.R. Chu, P.C. Qun, C.Z. Yong, J Cent. South Univ. **27**, 711 (2020)

22. R. Elliott, Mater. Sci. Eng. **65**, 85 (1984)

23. S.W. Yoon, J.R. Soh, H.M. Lee, B.J. Lee, Acta Mater. **45**, 951 (1997)

24. A. El-Daly, A. El-Taher, S. Gouda, J. Alloy. Compd. **627**, 268 (2015)

25. K. Prabhu, P. Deshapande, Mater. Sci. Eng. A **533**, 64 (2012)

26. W.R. Osorio, L.R. Garcia, L.C. Peixoto, A. Garcia, Mater. Des. **32**, 4763 (2011)

27. D.A.A. Shnawah, S.B.M. Said, M.F.M. Sabri, I.A. Badruddin, F.X. Che, Electron. Rel. **52**, 2701 (2012)

28. A.A. El-Daly, A.E. Hammad, J. Mater. Des. **40**, 292 (2012)

29. A.A. El-Daly, A.E. Hammad, G.A. Al-Ganainy, A.A. Ibrahiem, J. Mater. Des. **52**, 966 (2013)

30. A.A. El-Daly, A.A. Ibrahiem, M.A. Abdo, N.A.M. Eid, J. Mater. Sci.: Mater. Elec. **30**, 12937 (2019)

31. Q.S. Zhu, Z.G. Wang, S.D. Wu, J.K. Shang, J. Mater. Sci. Eng. A **502**, 153 (2009)

32. A.A. El-Daly, A.M. El-Taher, Mater. Des. **51**, 789–796 (2013)

33. I. Shohji, T. Yoshida, T. Takahashi, S. Hioki, J. Mater. Sci. Eng. A **366**, 50 (2004)

34. R. Mahmudi, A.R. Geranmayeh, H. Khanbareh, N. Jahangiri, J. Mater. Des. **30**, 574–580 (2009)

35. R.J. Mccabe, M.E. Fine, J. Metal. Mate. Trans. A **33A**, 1531 (2002)